Lawrence Berkeley National Laboratory
LBL Publications

Title
Correlative 3D Electron Tomography and Nanobeam 4D-STEM Mapping of Orientation and Strain in Welded Silver Nanowires

Permalink
https://escholarship.org/uc/item/33s7x20d

Journal
Small

ISSN
1613-6810

Authors
Radmilović, Vuk V
Ophus, Colin
Ercius, Peter
et al.

Publication Date
2026-10-24

DOI
10.1002/smll.76393

Copyright Information
This work is made available under the terms of a Creative Commons Attribution License, available at https://creativecommons.org/licenses/by/4.0/

Peer reviewed

eScholarship.org Powered by the California Digital Library
University of California

Correlative 3D Electron Tomography and Nanobeam 4D-STEM Mapping of Orientation and Strain in Welded Silver Nanowires

Vuk V. Radmilović[1*], Colin Ophus[2], Peter Ercius[3], Velimir R. Radmilović[4]

[1] University of Belgrade, Faculty of Technology and Metallurgy, Karnegijeva 4, 11020, Belgrade, Serbia
[2] Department of Materials Science and Engineering, Stanford University, Stanford, CA 94305, USA
[4] Lawrence Berkeley National Laboratory, Molecular Foundry, National Center for Electron Microscopy, Berkeley, CA 94720, USA
[5] Serbian Academy of Sciences and Arts, Knez Mihailova 35, 11000 Belgrade, Serbia

Abstract

A correlative analysis combining three-dimensional (3D) electron tomography and small convergence angle convergent-beam electron diffraction acquired in four-dimensional scanning transmission electron microscopy (4D-STEM) mode is used to investigate the structure, crystallographic orientation, and strain distribution in thermally welded silver nanowire (AgNW) junctions. High-angle annular dark-field scanning transmission electron microscopy (HAADF-STEM) tomography enables reconstruction of the asymmetric and faceted morphology of AgNW welds, revealing distinct ridge continuity and facet-specific junction geometries. Complementary diffraction mapping demonstrates orientation inheritance across the junction and crystallographic continuity within the welded region. Full-field strain maps derived from nanobeam 4D-STEM reveal minimal coherent strain (typically <0.5%) and small rotational distortions associated with nanowire bending. This multidimensional correlation of geometry, crystallography, and strain provides insight into weld formation mechanisms and interfacial behavior beyond the limits of conventional two-dimensional and localized atomic-resolution studies.

Introduction

Silver nanowires (AgNWs) are widely employed in transparent conductive films for next-generation flexible and stretchable electronics due to their excellent electrical conductivity, mechanical flexibility, and high optical transmittance [1,2,3]. Among the critical factors that influence device performance is the quality of nanowire–nanowire junctions formed during film fabrication. Poorly connected junctions lead to increased resistance and reduced mechanical integrity, thereby limiting large-area applicability and long-term stability [4].

Welding of AgNWs has emerged as a promising strategy to overcome these limitations by reducing contact resistance and enhancing mechanical robustness through the formation of welded junctions [5]. In the context of flexible electronics, such welded networks contribute significantly to the reliability and performance of devices under bending, stretching, or thermal/bias cycling [6]. Previous work, including our own studies [7,8,9,10,11], has illuminated the atomic-scale features of these welds, elucidating neck formation, wetting behavior, epitaxial growth, and the thermodynamic and kinetic factors that drive junction formation.

While these studies have yielded valuable insights, they have predominantly relied on two-dimensional projection imaging and localized analysis, limiting access to the full three-dimensional junction geometry and its coupling to crystallographic orientation and strain. In particular, the three-dimensional geometry of the welds and how it couples with crystallographic orientation and local strain distribution across the junction remains poorly

understood. This represents a critical knowledge gap, as these factors directly affect the electrical, thermal, and mechanical performance of the nanowire network.

To address this, the present study adopts a correlative approach that combines electron tomography and diffraction-based orientation and strain mapping acquired in four-dimensional scanning transmission electron microscopy (4D-STEM) mode. In this work, diffraction data were collected using a nanometer-scale electron probe with a finite convergence semi-angle, producing disk-shaped Bragg reflections. For clarity, this approach is referred to here as small-convergence-angle convergent-beam electron diffraction (CBED) acquired in 4D-STEM nanobeam mode [12,13,14] i.e. nanobeam 4D-STEM. By integrating these approaches over extended regions, we aim to directly relate weld morphology with underlying crystal orientation relationships and internal strain fields.

While conventional two-dimensional HAADF-STEM imaging provides valuable contrast related to thickness and composition, it is fundamentally limited in resolving the true three-dimensional geometry of welded AgNW junctions. Features such as surface faceting, angular alignment, ridge continuity, and spatial orientation cannot be reliably inferred from projection images alone, motivating the use of HAADF-STEM tomography for quantitative 3D reconstruction. HAADF-STEM tomography is particularly powerful for 3D analysis of nanostructures, as high-angle incoherent scattering provides strong contrast sensitivity to both composition and specimen thickness [15,16,17]. In the case of AgNW junctions, which consist solely of Ag atoms, contrast differences arise purely from variations in projected thickness.

In addition to three-dimensional imaging, understanding the crystallographic orientation and strain distribution within welded nanowire junctions requires spatially resolved diffraction-based techniques. Nanobeam 4D-STEM nanobeam mode provides a powerful complement to tomographic reconstruction, enabling nanometer-scale mapping of crystal orientation [18] and lattice distortion within complex geometries. Strain at this scale [19] can be evaluated using several TEM-based methods [20] including: Convergent-beam electron diffraction (CBED) [21], Nano-beam electron diffraction (NBED) [22]; HRTEM/STEM [23] and Dark-field electron holography (DFEH) [24]. However, HRTEM or HRSTEM imaging was avoided in this study due to the structural complexity of the junction, including mistilt, overlapping twin domains, and the need for fully resolved atomic columns across the entire weld. Given the relatively large thickness of the welded region, typically exceeding 200 nm, nanobeam 4D-STEM was selected as the most appropriate method for strain evaluation. By scanning the region and applying automated analysis via a dedicated MATLAB algorithm, we efficiently extracted high-resolution maps of local lattice parameter changes and crystal orientation relative to pristine segments of the AgNWs. When combined with tomographic data, this correlative approach provides detailed insights into how structural geometry and crystallography jointly govern weld formation and stability.

Our objective is to establish how geometry, crystallography, and strain converge at AgNW junctions to determine nanoscale structural integrity and potential functional performance. This multimodal analysis offers a more holistic understanding of AgNW weld behavior, complementing earlier atomic-scale studies [25,26] and providing a structural framework for understanding welded nanowire junction behavior. The findings not only bridge the gap between local atomic-scale phenomena and mesoscopic junction behavior but also highlight the value of correlating multiple imaging modalities to interpret nanostructure–property relationships in complex networks.

Materials and Methods

For tomography characterization, AgNWs in water (Cambrios® ClearOhm ink) with an average diameter of ~30 nm were drop cast onto lacey carbon 300 mesh copper TEM grid and

dried. Subsequently, the grid was held for 30 seconds at 210 °C on a hot plate (AgNW side up) and then immediately inserted into the transmission electron microscope. Tilt series of HAADF-STEM images with 512 × 512 pixels for tomographic reconstructions were acquired automatically on a ThermoFisher Titan 80-300 electron microscope called the TitanX operated at 200 kV, at a semi-convergence angle of 10 mrad and an inner collection angle of 60 mrad. Images were recorded using the automated FEI® tomography software, with a dwell time of 6 µs from -70 to +70° in 1° intervals, without fiducial markers, with a probe step size of 0.57 nm. The dose rate was $\sim 10^5$ e^-/nm^2s. Compensations for sample drift, as well as image focus were used between successive image acquisitions. Three-dimensional reconstructions were performed from the 141 image tilt series by applying an algorithm for weighted back-projection (WBP) described in foundational works on STEM and EFTEM tomography of nanostructures [27,28,29]. Three-dimensional reconstructions were refined using the simultaneous iterative reconstruction technique (SIRT) [30], using the ASTRA-toolbox 2D CUDA-SIRT algorithm with 25 iterations. The reconstruction was segmented via custom code using the visualization tool kit 8.1.0 (VTK) Python distribution. All visualizations were prepared in Tomviz v1.4.0.

Post-processing and visualization were accomplished using Tomviz and quantitative analysis was accomplished using custom scripts in Python. Samples investigated for orientation and strain distribution consisted of thermally welded AgNW junctions prepared under identical conditions to those used for tomography, but employing nanowires with an average diameter of approximately 100 nm to ensure sufficient diffracted signal for nanobeam-based analysis. 4D-STEM data were acquired on the 300 kV aberration-corrected Thermo Fisher Titan 80-300 TEAM I microscope, operated in STEM mode with a sub-nanometer probe formed using a 10 µm condenser aperture and a 10 mrad convergence semi-angle. Diffraction patterns were recorded at 400 frames/s using a Gatan K2 pixelated detector. Diffraction datasets were acquired over a 128 × 128 probe-position grid, corresponding to a scan step size of 5–7 nm. During acquisition, the electron probe was rastered across the selected region, and a nanobeam 4D-STEM pattern was recorded at each probe position, yielding a four-dimensional diffraction dataset. The selected convergence semi-angle produced non-overlapping diffraction disks, enabling reliable determination of both lattice rotation and elastic strain from disk displacement analysis. Orientation and strain maps were calculated by detecting diffracted beam positions using custom MATLAB® routines based on established disk-displacement methodologies [20,31]. Strain values were evaluated relative to adjacent unwelded segments of the nanowires, serving as a reference lattice. The standard deviation of the calculated coherent strain was ±0.1%. Map intensity reflects the relative strength of the indexed diffraction signal.

For orientation mapping, up to 40 diffraction disks were detected and indexed, followed by classification into several crystallographic orientation families, including <112>, multiple <110> type orientations, <111> and an undefined class corresponding to patterns with insufficient reflections for reliable indexing. Any pixels that had diffraction intensity from one of the five patterns above some threshold (10% of the maximum signal) were classified as "the same". The intensity of the main plot shows how strongly the given peaks (insets in Figure 5) were measured.

Results and discussion

Figure 1 is a HAADF-STEM image of a welded junction between two AgNWs, recorded at 0° tilt angle. White arrows indicate diameters of 35.4 nm and 40.7 nm for the two AgNWs. Acquisition of the 2D tilt series used for tomographic reconstruction was performed from the dotted square area noted in this image.

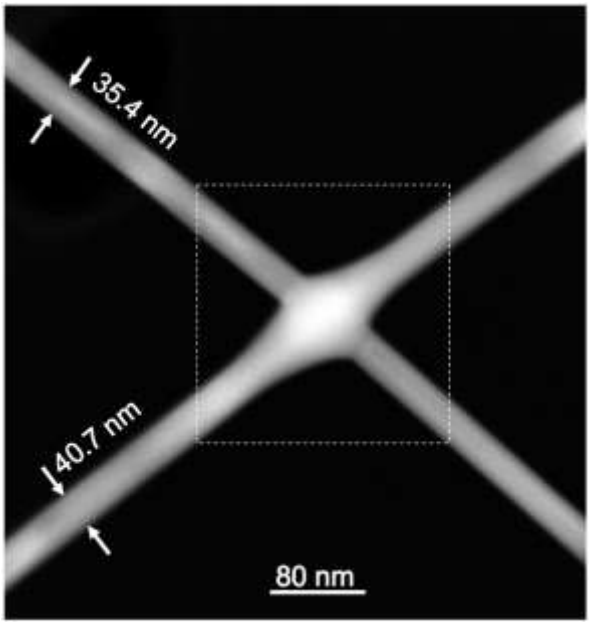


Figure 1. HAADF-STEM image of welded junction between two AgNWs. White arrows indicate NW diameters.

Figure 2 represents a 3D reconstructed volume of the section noted by the white dotted square in Figure 1. The reconstruction exhibits features indicative of a faceted morphology and five-fold symmetry of two AgNWs creating a nanoweld after annealing for 30 seconds at 210°C. It can clearly be seen that the central ridge in the thicker AgNW remains uninterrupted along the entire length, while the central ridge in the thin AgNW stops at the nanoweld, indicated by white arrows. Such ridge termination and continuity cannot be inferred unambiguously from 2D projection images or localized atomic-resolution observations, which have primarily been used in previous studies of thermally welded AgNW junctions [32,33].

By analyzing the HAADF-STEM image of the welded junction recorded at 0° tilt angle, shown in Figure 1, as well as at different tilt angles, ranging from -70° to +70°, it is evident that the weld is of highly anisotropic shape. However, projection imaging alone cannot uniquely determine whether this apparent anisotropy arises from true three-dimensional geometry or from overlap effects along the beam direction, a limitation well recognized in earlier studies of nanowire junctions based on two-dimensional imaging [34,35].

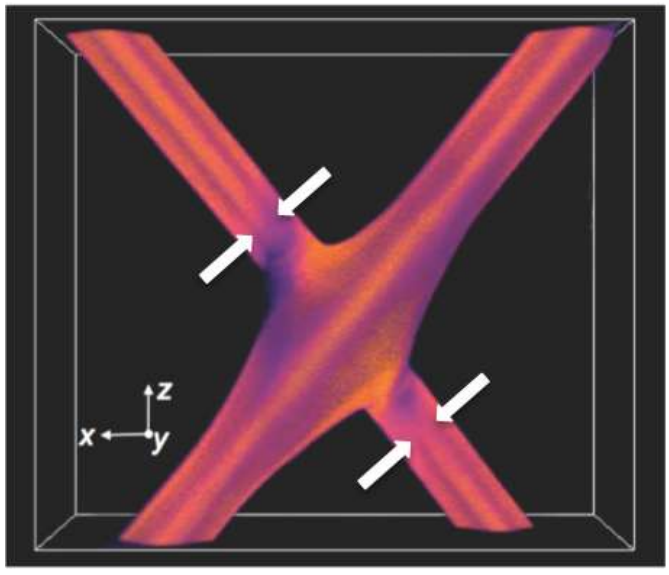


Figure 2. 3D structure of the reconstructed welded junction between two AgNWs. White arrows indicate central ridge of thinner NW close to the nanoweld, terminated due to sharp edge dissolution.

Figures 3a,b show two 180°-separated views of the SIRT tomographic surface rendering of the welded AgNWs. From these two images, it is clear that both AgNWs are characterized by the presence of five surface facets and a pentagonal cross-section. It is also evident that the top corner of the thinner NW was in contact with the bottom flat facet of the thicker NW before heating was performed. From Figures 1 and 2 it is not possible to elucidate the type of crystallographic facets through which the NWs are in contact, but based on the tomographic reconstruction, shown in Figures 3a and b, it can be concluded that they are of {100} type, consistent with the known faceting behavior in pentagonally twinned AgNWs [36,37].–The present 3D tomographic reconstruction therefore provides direct structural information that complements and extends earlier 3D studies of AgNW networks that lacked junction-level structural resolution [38].

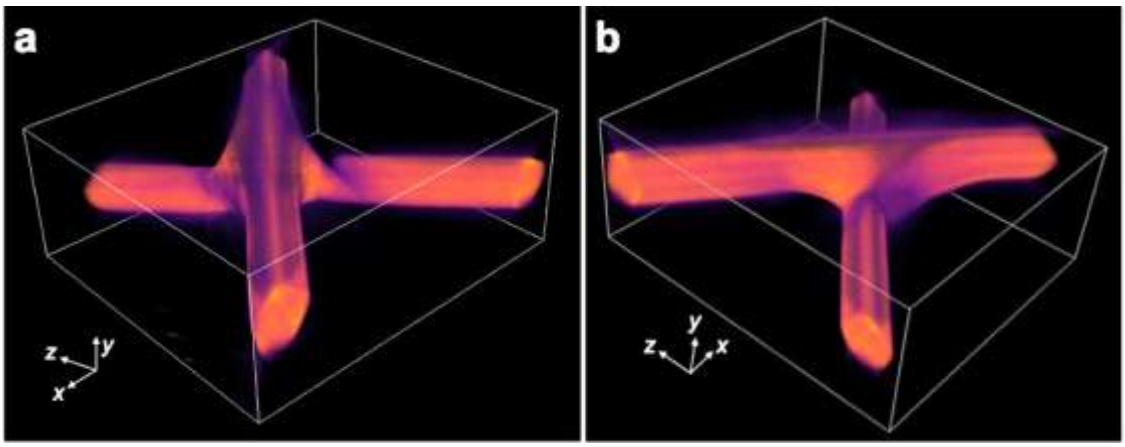


Figure 3. 3D volume renderings of welded AgNWs, shown from different viewpoints; a) is rotated 180° with respect to b); Cartesian coordinates are indicated by white arrows.

A HAADF-STEM image of the welded region between two AgNWs is shown in Figure 4a, while the pattern (Figure 4b), taken from the welded zone indicated by the red circle in the HAADF-STEM image, is also shown. The pattern, taken close to the [$\bar{1}12$] zone axis, confirms <110> growth direction of the thinner AgNW, as routinely determined using disk-based nanobeam 4D-STEM orientation analysis [14,39].

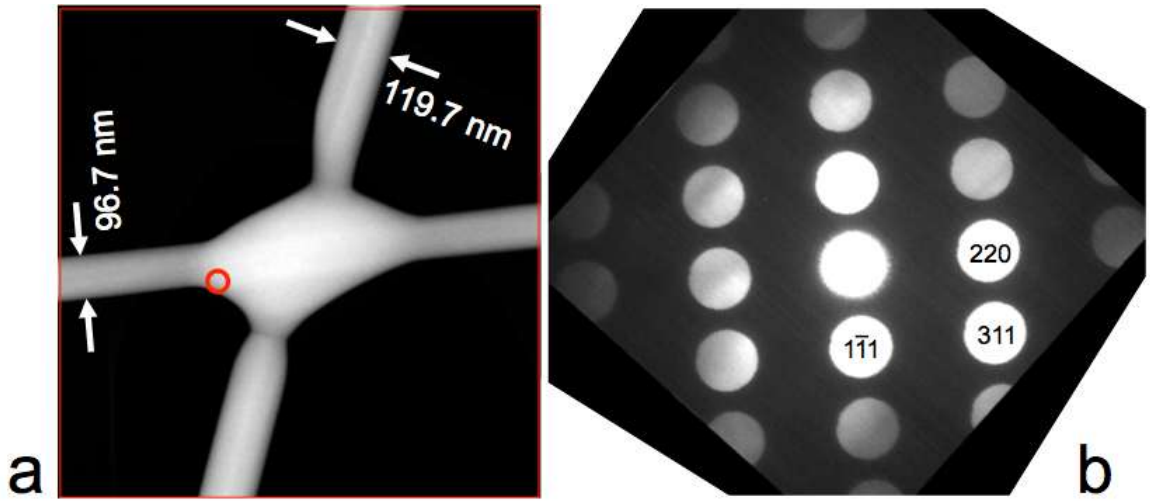


Figure 4. a) HAADF-STEM image of welded AgNWs with indicated diameters, b) 4D-STEM CBED pattern taken close to $[\bar{1}12]$ zone axis from the region indicated by red circle in a).

Figure 5 shows orientation maps, demonstrating specific alignment of twin segments within both AgNWs, as well as the welded zone. Each map shows the strength of the diffraction signal, using the color-map: black, purple, red, orange, yellow and white, where white represents areas with the highest signal and black represents areas with no diffraction signal, or too low to classify.

The light blue regions represent pixels where diffraction intensity exceeded the minimum threshold for orientation classification (see Methods). These relative values are arbitrary, changing from pattern to pattern and are just a representation of how much signal is in a given area. Orientations of 4D-STEM patterns for corresponding AgNW segments and the welded zone are as follows: <112> in Figure 5a, <110> in Figures 5c and e, <111> in Figure 5d and <110> in Figure 5e while for Figure 5b the 4D-STEM pattern displays <112> as well as several other mixed orientations with very weak signals. These signals likely arise from local thickness variations, dynamical scattering and slight crystal mistilt within the welded region. Neighboring pixels were classified as belonging to the same orientation when their detected diffraction peak configuration matched the corresponding reference pattern above a 10% intensity threshold. These orientation maps show that the welded zone has the same crystallographic orientation as the NW to which it is attached. Such disk-based orientation mapping is a well-established capability of 4D-STEM, which enables simultaneous access to crystallographic orientation and lattice distortion over extended regions [18,40,41].

Recent 4D-STEM studies of crystalline interfaces have similarly demonstrated that diffraction enables reliable identification of orientation inheritance and subtle misorientations over extended regions where atomic-resolution imaging is impractical, particularly in the presence of thickness variations and local mistilt [14].

Orientation maps were constructed by classifying disk-based diffraction peaks into discrete crystallographic orientations using an intensity-based threshold, while accounting for variations in diffraction intensity caused by thickness and local mistilt.

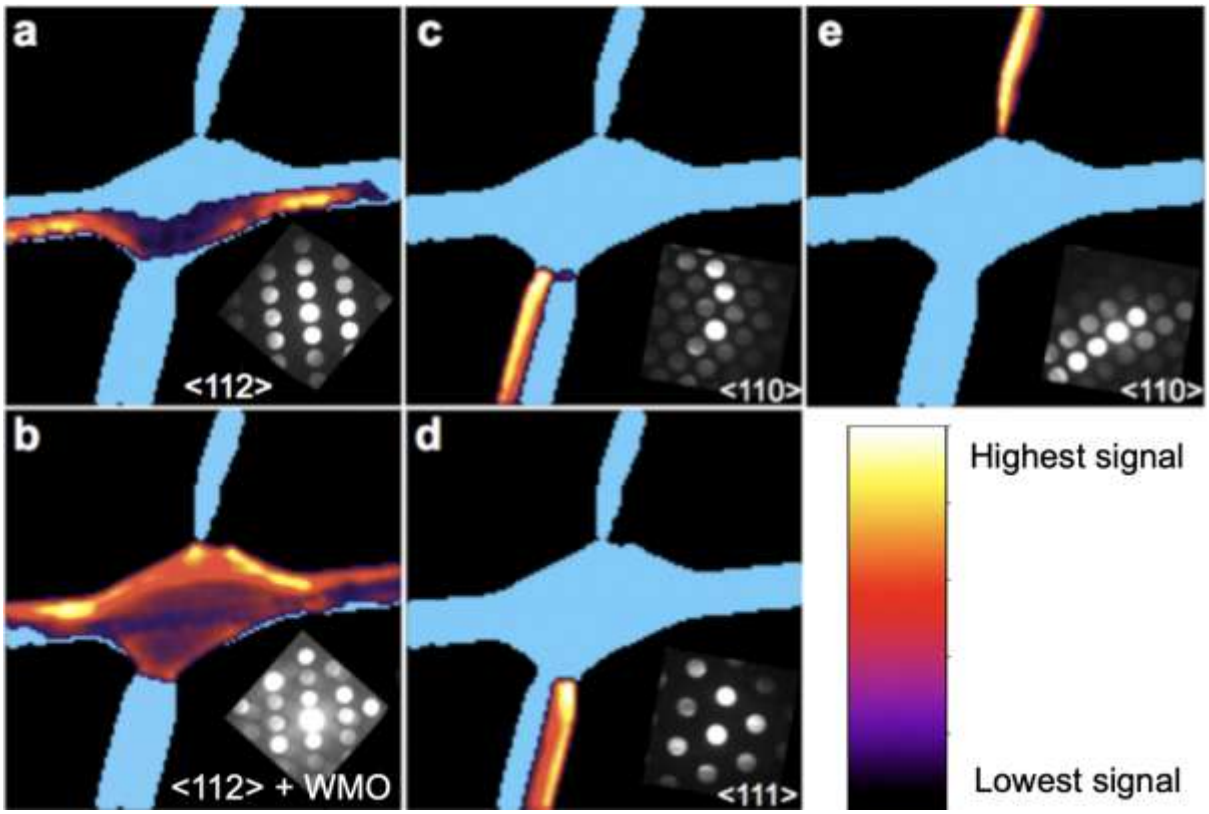


Figure 5. Orientation maps for various sections of both AgNWs and the welded zone; a) and b) are maps of thinner NW and the welded zone; c) and d) are maps of left and right sections of the thicker NW, below the welded zone; e) Map of left section of thicker NW above the welded zone; light blue color indicates area where diffraction signal > 0, colorbar indicates diffraction signal intensity with black depicts area with no diffraction signal, white color represents area with highest signal; Insets represent 4D-STEM patterns with noted orientations (WMO refers to weak mixed orientations).

Due to a relatively large field of view, ~1 μm^2, bending and twisting of AgNWs, as a result of drop cast deposition, resulted in a substantial mistilt of the crystal structure orientation. The relatively large scan area also enables orientation and strain mapping across the full diameter of thicker nanowires, offering a significant advantage over atomic-resolution electron microscopy, which is limited to thin, well-aligned regions. This can be clearly seen in Figure 6a, where rotation angle θ can differ by more than 3° for various segments of the same NW. Such orientation variations are characteristic of mechanically induced bending and twisting in freestanding metallic nanowires and should not be interpreted as coherent lattice strain. Diffraction-based approaches are particularly well suited to distinguish rigid-body rotation from elastic strain contributions in these cases. [40]. Variation of θ angle value is present even within the same segments of the NW, as shown in Figures 6b, c and d, but it is significantly smaller, usually less than 0.5°. Further improvements in strain and orientation precision are expected through advanced analysis strategies for 4D-STEM datasets, as demonstrated in recent algorithm-driven studies [40]. Under such conditions, nanobeam 4D-STEM provides a practical compromise between spatial resolution and diffraction reliability, enabling statistically meaningful strain and orientation mapping in specimens that exceed the thickness limits typically required for atomic-resolution imaging [39].

Overall, no significant strain fluctuations were observed across the AgNWs and their welded junctions, suggesting lattice continuity and structural coherence at the nanoscale. It

should be noted that, as highlighted in comparative 4D-STEM strain studies, measured strain profiles near interfaces can be broadened or affected by probe tails and dynamical diffraction effects, which may modestly influence the apparent strain distribution even in nominally coherent regions [42].

This behavior contrasts sharply with equilibrium pentagonally twinned metallic nanostructures, in which significant tensile and shear strain components—often approaching or exceeding ~1% are required to accommodate the intrinsic disclination associated with five-fold symmetry. In comparison, the welded AgNW junctions investigated here exhibit minimal coherent strain, indicating that junction formation proceeds primarily through surface diffusion and crystallographic registry rather than bulk lattice distortion.

Figure 6 represents color-coded maps of coherent strain and lattice distortion distribution within AgNWs and nanoweld region. For each area of investigated sample, both for AgNWs and the welded zone, 2D maps of ε_{xx} (horizontal strain), ε_{yy} (vertical strain) and ε_{xy} (shear strain) are shown as well as maps of rotational angle (θ) distribution. Because of the large AgNW diameters, coherent strain could only be evaluated in regions where the diffraction disks remained sufficiently sharp and well separated for reliable localization. Across all analyzed regions (Fig 6a-c), ε_{xx}, ε_{yy}, and ε_{xy} remain predominantly within ±0.1%, rarely exceeding ±0.5%, while rotational variations are confined to <0.5° within individual nanowire segments. Reliable extraction of such small strain magnitudes from nanobeam 4D-STEM datasets requires robust localization of diffraction disks and stable lattice fitting procedures, which have been shown to remain effective even in the presence of partial disk overlap and dynamical scattering [41]. Comparable magnitudes of nanoscale elastic strain have been reported in other crystalline systems using 4D-STEM-based diffraction analysis, confirming that subtle strain fields of this order are both experimentally resolvable and physically meaningful. The dominance of small rotational components over coherent elastic strain further supports a deformation mode governed by rigid-body bending rather than disclination-mediated lattice distortion. Recent high-precision studies have emphasized the importance of explicitly separating rotational and tensile strain components to avoid overestimating elastic deformation in nanoscale systems [39]. Insets in Figures 5a-d represent patterns of corresponding AgNW segments and welded zone with orientations noted in Figure 5. In Figure 6a, two patterns are present, one corresponding to part of thicker NW above the welded zone while the other corresponding to part of thicker NW below the welded zone.

It should be noted that the right-hand part of the NW above the weld in Figures 5 and 6 is missing. This is a consequence of the region being too tilted i.e. if the NW is tilted more than 3°, the diffraction condition deviates sufficiently from the selected zone axis that the corresponding diffraction disks can no longer be reliably indexed for orientation and strain analysis. This does not mean that an AgNW segment is missing, but that Figures 5 and 6 present maps of areas where diffraction signal is present. The HAADF STEM image in Figure 4 clearly shows the preserved integrity of the whole NW above the weld.

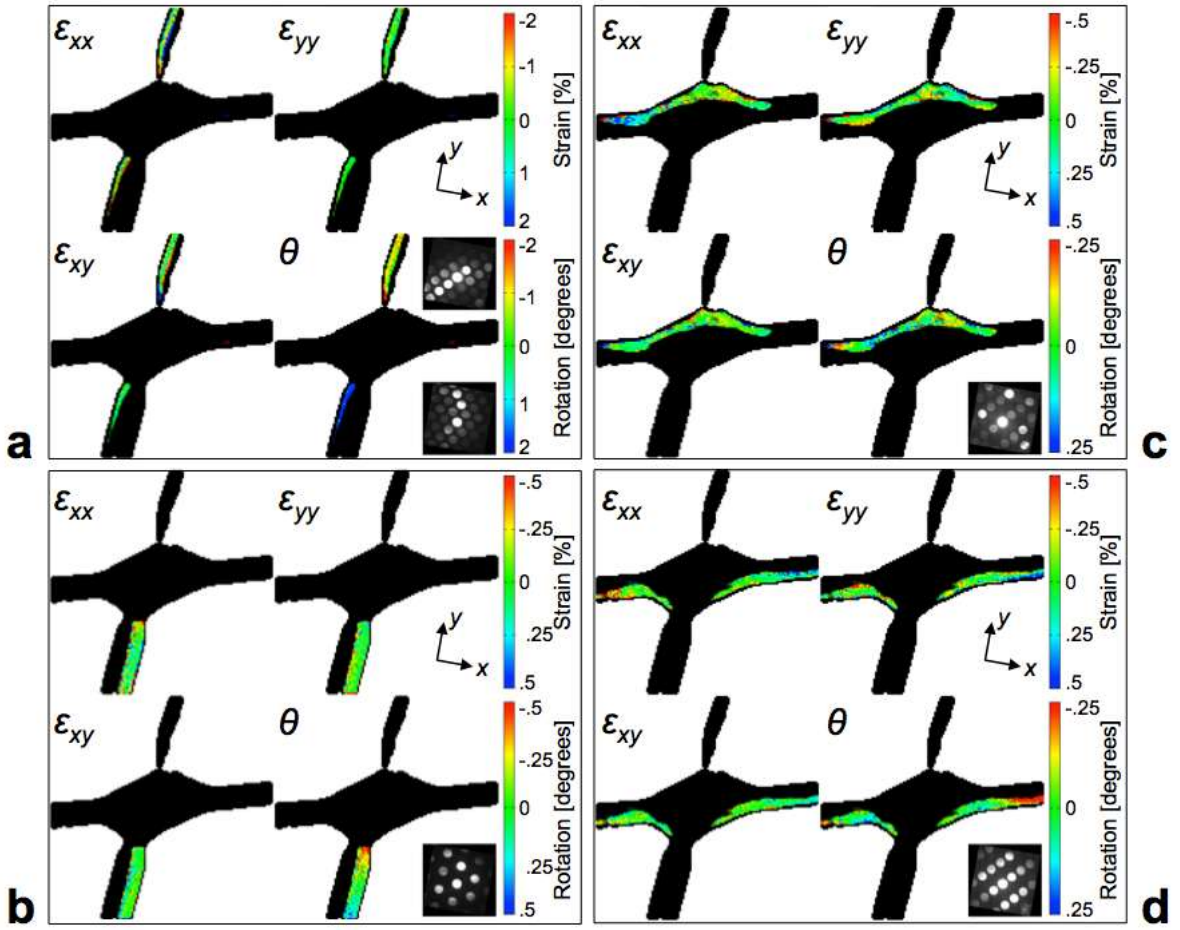


Figure 6. Color-coded maps of coherent strain (ε_{xx}, ε_{yy}, ε_{xy}) and lattice rotation angle (θ) distribution within AgNWs and the welded zone; black color indicates contour of investigated sample; Insets represent nanobeam 4D-STEM patterns corresponding to indicated color-coded areas. Also noted are Cartesian coordinates.

The combined orientation and strain mapping reveals that thermally welded AgNW junctions preserve crystallographic continuity across the weld, while accommodating geometric misalignment primarily through rigid-body rotation rather than elastic lattice distortion. Such orientation inheritance across a welded interface is consistent with epitaxial-like regrowth mechanisms driven by surface and grain-boundary diffusion during thermal annealing. Similar crystallographic continuity has been inferred previously from atomic-resolution FFT analysis of AgNW junctions, although only over highly localized regions.

This crystallographic continuity is consistent with an epitaxial-like regrowth mechanism driven by surface and grain-boundary diffusion during thermal annealing. In contrast, the present nanobeam 4D-STEM approach enables orientation mapping across extended areas, including thick nanowire segments and the full weld volume [14,18,39].

Coherent strain within both nanowires and the welded junction remains negligible.

Importantly, the dominance of rotational components over coherent elastic strain distinguishes the deformation behavior of welded AgNW junctions from equilibrium pentagonally twinned metallic nanostructures [8,32], where significant tensile and shear strains often approaching or exceeding ~1% are required to accommodate the intrinsic disclination associated with five-fold symmetry. In the present case, the absence of pronounced strain accumulation at the weld indicates that junction formation proceeds primarily through surface

diffusion and crystallographic registry, rather than through bulk lattice distortion or disclination-mediated strain accommodation.

Taken together, these results demonstrate that thermally welded AgNW junctions maintain crystallographic integrity while accommodating geometric misalignment through bending and rotation, resulting in negligible residual elastic strain. By correlating three-dimensional morphology with full-field orientation and strain mapping, this work extends beyond prior two-dimensional and localized atomic-resolution studies and provides a comprehensive structural framework for understanding nanowire weld formation. The combination of electron tomography and nanobeam 4D-STEM thus offers a powerful and broadly applicable strategy [43,44] for analyzing complex nanostructured junctions that exceed the thickness and alignment constraints of conventional high-resolution imaging.

CONCLUSION

This work demonstrates the power of a correlative approach that integrates 3D electron tomography, nanobeam 4D-STEM based orientation mapping, and strain analysis to study welded AgNW junctions. The tomographic reconstruction revealed anisotropic weld geometry of two nanowires in contact through different curvature sections, while orientation maps confirmed lattice continuity across the junction. Strain mapping further showed minimal residual deformation, suggesting mechanically robust interfaces with implications for favorable electrical conductivity, needed for electronic applications. This procedure provides a multi-dimensional structural and crystallographic framework for understanding nanowire welding mechanisms, relevant to the design of transparent and flexible electrode architectures. By combining imaging and diffraction modalities, this work sets a foundation for rational design and engineering of next-generation nanowire-based electronic and optoelectronic devices.

Acknowledgements

This work was supported by the Ministry of Science, Technological Development and Innovation of the Republic of Serbia (Contract No. 451-03-34/2026-03/200135) and Serbian Academy of Sciences and Arts (Grant No. F141). ChatGPT was used in the final revision to improve formulations and shorten the text. Work at the Molecular Foundry was supported by the Office of Science, Office of Basic Energy Sciences, of the U.S. Department of Energy under Contract No. DE-AC02-05CH11231.

References

[1] J.S. Meena et al., Advanced Material Technologies 8(2023) 2300602.
[2] L. Zhang, et al. Journal of Nanostructure in Chemistry 11 (2021) 323–341.
[3] M.R. Azani et al., Advanced Energy Materials, 10 (2020) 2002536
[4] L. Gan et al., Critical Reviews in Solid State and Materials Sciences 50 (2025) 1–53.
[5] Y. Ding et al., Applied Materials Today 20 (2020) 100634.
[6] C. Li et al., Journal of Physics D: Applied Physics 58 (2025) 103001.
[7] E. C, Garnett et al., Nature Materials 11 (2012) 241–249.
[8] V.V. Radmilovic et al, Nanotechnology 28 (2017) 385701.
[9] H. Kang et al., ACS Nano 12 (2018) 4894–4902.
[10] G. Liu et al., Nano Research 15 (2022) 2582–2591.
[11 V-T Nguyen et al., Materials Today Communications 34 (2023) 105051.
[12] K. Bustillo et al., Accounts of Chemical Research 54 (2021) 2543−2551.

[13] G. Zhu et al., Nano Letters 25 (2025) 13526–13532
[14] C. Ophus, Microscopy and Microanalysis 25 (2019) 563–582.
[15] S.J. Pennycook et al., Ultramicroscopy 37 (1991) 14–38.
[16] S.J. Pennycook, Ultramicroscopy 30 (1989) 58–69.
[17] C. Ophus, Annual Review of Materials Research 53 (2023) 105–141.
[18] A.C. Diebold et al., Microscopy and Microanalysis, 31 (2025) ozaf019.
[19] M.J. Hytch et al., MRS Bulletin, 39 (2014) 138-146.
[20] A. Beche et al. Ultramicroscopy 131 (2013) 10-23.
[21] Uesugi et al Ultramicroscopy 261 (2024) 113966.
[22] H. Ding et al., Acta Materialia 287 (2025) 120778.
[23] D. Nelli et al., Advances in Physics: X 8 (2023) 2127330.
[24] L. Niermann et al., Ultramicroscopy 271 (2025) 114122.
[25] S. Sun et al., Physics Review Letters 128 (2022) 015701.
[26] X. Qi et al., ACS Nano 13 (2019) 4647–4656.
[27] P. Midgley et al., Ultramicroscopy 96 (2003) 413-431.
[28] P. Midgley et al., Nature Materials 8 (2009) 271–280.
[29] P. Ercius et al., Advanced Materials 27 (2015) 5638–5663.
[30] N. Baba et al., Microscopy 72 (2023) 111–134.
[31] T.C. Pekin et al., Ultramicroscopy 176 (2017) 170–176.
[32] N. Schrenker et al., ACS Nano 15 (2021) 362−376.
[33] A. Teymouri et al., ACS Applied Nano Materials 3 (2020) 3205–3213.
[34] H. Blumtritt et al., Nanotechnology 25(2014) 435704.
[35] J.H. Song et al., Advanced Materials Interfaces, 5(2018) 1800250.
[36] A. Eggeman et al., Nature Communications 6 (2015) 7267.
[37] R.L.S. Tan et al., Journal of American Chemical Society 138 (2016) 10770–10773.
[38] S. Englisch et al., Microscopy and Microanalysis 24 (2018) 558–559.
[39] P. Zeltmann et al., Microscopy and Microanalysis, 26 (2020) 1724–1726.
[40] R. Yuan et al., Ultramicroscopy 231 (2021) 113256.
[41] S. Wang et al, Ultramicroscopy 236 (2022) 113513.
[42] C. Mahr et al, Ultramicroscopy 221 (2021) 113196.
[43] M. Bolhuis et al., Small Science 4 (2024) 2300249.
[44] Y. Song et al., Nature Communications 16 (2025) 11535.